

Space Weather

RESEARCH ARTICLE

10.1029/2019SW002234

Key Points:

- Power system coefficients derived from a time series of GIC and geoelectric field measurements are frequency dependent
- A GIC model with frequency-dependent system coefficients provides significantly better estimates of GIC than a frequency-independent model
- Data-derived power system coefficients may differ significantly with those computed using power system configuration information

Correspondence to:

R. S. Weigel,
 rweigel@gmu.edu

Citation:

Weigel, R. S., & Cilliers, P. J. (2019). An evaluation of the frequency independence assumption of power system coefficients used in geomagnetically induced current estimates. *Space Weather*, 17, 1674–1688. <https://doi.org/10.1029/2019SW002234>

Received 22 APR 2019

Accepted 5 OCT 2019

Accepted article online 15 OCT 2019

Published online 17 DEC 2019

An Evaluation of the Frequency Independence Assumption of Power System Coefficients Used in Geomagnetically Induced Current Estimates

R. S. Weigel¹  and P. J. Cilliers² 

¹Space Weather Lab, George Mason University, ²South African National Space Agency

Abstract A common assumption used when estimating geomagnetically induced currents (GICs) in a power system given a time series of nearby direct measurements or indirect estimates of the horizontal geoelectric field components $E_x(t)$ and $E_y(t)$ on Earth's surface is that the system is resistive. That is, the approximation $GIC(t) = a_o E_x(t) + b_o E_y(t)$ (Model 1) is used, where a_o and b_o are frequency-independent power system coefficients. A first test of this assumption is made using GIC measurements in a 187 kV transformer connected to a ~100 km power line in Memanbetsu, Japan and geoelectric field measurements made at the Memanbetsu Magnetic Observatory ~9 km away. A second model (Model 2) is obtained using a frequency domain generalization of Model 1: $GIC(\omega) = a(\omega)E_x(\omega) + b(\omega)E_y(\omega)$. The coefficients $a(\omega)$ and $b(\omega)$ are shown to be frequency-dependent, and this model provides significantly better estimates of the measured GIC than Model 1. Based on results using a simulated geoelectric field, it is suggested that the measurement-derived frequency dependence of the system coefficients may be explained by spatial variations in the spectrum of the geoelectric field over the spatial extent of the power system. It is also shown that further improvements over Model 2 can be made using frequency-dependent models with the geomagnetic field as an input.

1. Introduction

Geomagnetically induced currents (GICs) are electric currents in conducting systems that are due to electric fields near the Earth's surface. Time-varying electric and magnetic fields at Earth's surface are driven by time variations in ionospheric currents on time scales of seconds to hours (Ohtani et al., 2000) and the movement of Earth's surface relative to slow-varying current systems in Earth's ionosphere that are near stationary relative to the Sun (Stening and Winch, 2013). Of particular interest are currents induced in electric power systems because they can lead to system degradation, disruption, and failure (Albertson et al., 1993; Gaunt, 2014; NERC, 2012). Accurate estimation of GIC magnitudes is important for power system design, retrospective analysis, and mitigation of the impacts of space weather on power systems (Gaunt, 2014; Molinski, 2002; NERC, 2012; Thomson et al., 2010).

A common assumption made in estimates of GIC in an electric power system using either a measured or estimated time series of the horizontal geoelectric field at Earth's surface, $\mathbf{E}(t)$, is that the power system is resistive or quasi-DC in the sense that the relationship $GIC(t) = a_o E_x(t) + b_o E_y(t)$ holds (Albertson et al., 1981; Lehtinen and Pirjola, 1985). In this case, estimates of the coefficients a_o and b_o can be easily made from the data using linear regression when contemporaneous measurements of $GIC(t)$ and $\mathbf{E}(t)$ are available, or by using information about the connectivity of the power lines and values of the conductor and transformer resistances using DC circuit methods (e.g., Boteler, 2014; Boteler & Pirjola, 2014, 2017). This quasi-DC assumption has been used or stated in many GIC-related works, for example, Pulkkinen et al. (2007), Wik et al. (2008), Pirjola (2009), Pulkkinen et al. (2010), Ngwira et al. (2011), Horton et al. (2012), Viljanen et al. (2012), Overbye et al. (2012), Marshall et al. (2013), Liu et al. (2014), Zheng et al. (2014), Watari (2015).

In this work, we use a unique dataset in which time series measurements of \mathbf{E} and the surface horizontal geomagnetic field, \mathbf{B} , were made near a site where GIC was being measured in an electric power system. We first estimate the system coefficients a_o and b_o from data using conventional methods, in which they are

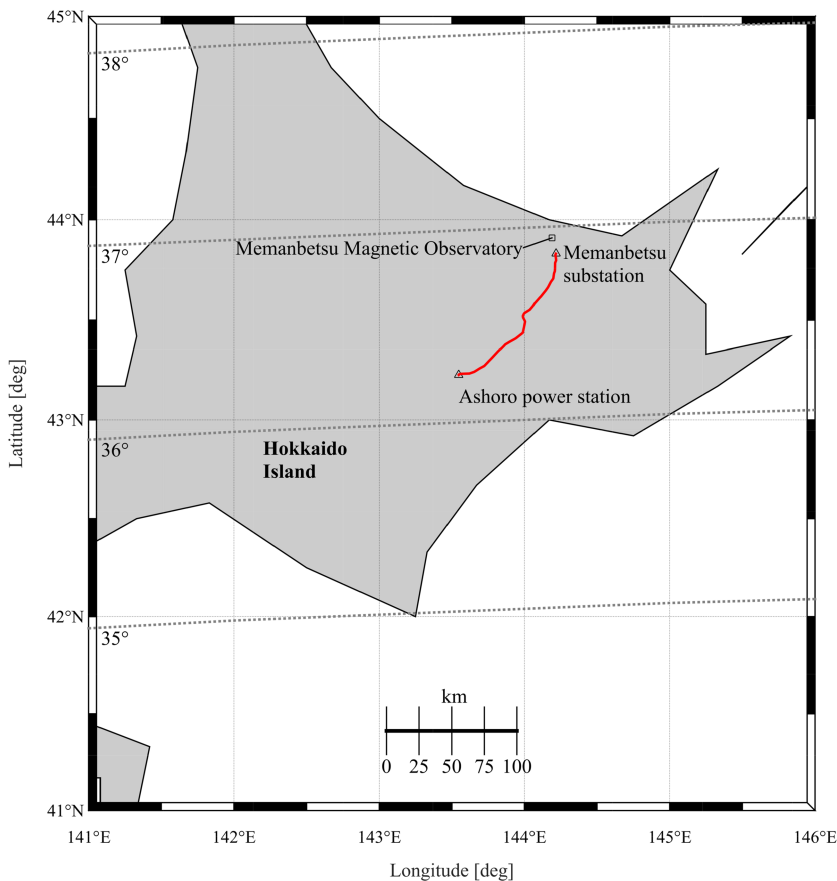


Figure 1. Locations of measurement sites for GIC, at the Memanbetsu substation, and the geoelectric and geomagnetic field measurement site at Memanbetsu Magnetic Observatory. The red line corresponds to the path of the 187 kV power line. The distance from the observatory to the Memanbetsu substation is ~9 km and dotted lines are Apex geomagnetic latitudes (Richmond, 1995) in 2015.

modeled as frequency independent. Then, we use a model in which the system coefficients are allowed to be frequency dependent, compute the frequency dependence, and compare this model's ability to represent GIC with the traditional frequency-independent model. Two additional frequency-dependent models are considered that require only the geomagnetic field as an input and they are shown to be significantly better at estimating GIC than the models that use the geoelectric field as an input.

2. Data

The 1-second-cadence GIC data used span a total of 35 days across 10 intervals that start and end at midnight Japan Standard Time (JST) and are listed in Table A1. These data have been presented previously in Watari et al. (2009) and Watari (2015). These time intervals are those for which GIC data was made available except for 3 days for which there were obvious problems with either the electric field or GIC measurements. The GIC dataset includes 1 s raw data and 1 Hz low-pass-filtered raw measurements and the results presented are for the 1 Hz low-pass-filtered GIC measurements.

GIC was measured in a grounded neutral point of a Y-connected three-phase transformer connected to the 187 kV bus at the Memanbetsu substation of the Hokkaido Power Co. The 187 kV line extends from the Ashro substation to the Memanbetsu substation, which are both grounded. Memanbetsu is an end-point of the 187 kV line.

One-second-cadence electric and magnetic field measurements from Memanbetsu Magnetic Observatory (geodetic latitude: 43.910° N, geodetic longitude: 144.189° E) were obtained from the Japan Meteorological Agency data portal. The locations of the observatory and substations are shown in Figure 1.

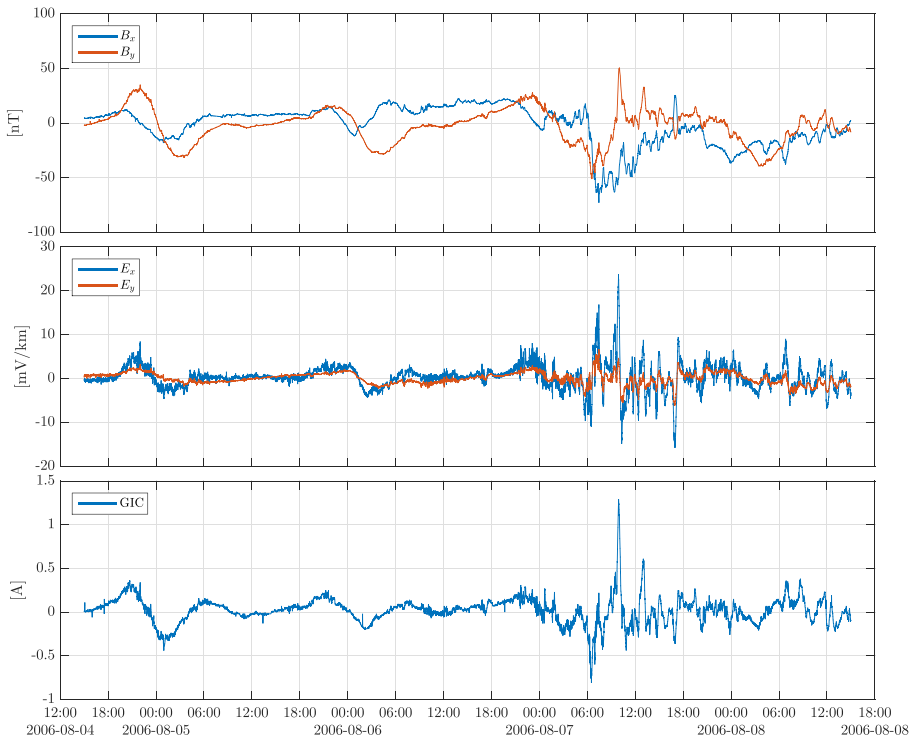


Figure 2. (Top) Geomagnetic field measured at the Memanbetsu Magnetic Observatory (MMB). (Middle) Geoelectric field measured at the Memanbetsu Magnetic Observatory (MMB). (Bottom) GIC measurements at Memanbetsu substation. The subscripts x and y correspond to Geographic North and East, respectively, the date labels are for Universal Time, and the average has been subtracted from each time series.

Data for the time span of 2006-08-04T15:00Z through 2006-08-08T15:00Z are shown in Figure 2. The GIC data were provided as 1-day files that start at midnight JST and the times shown in Figure 2 are Universal Time.

Spikes in the electric field measurements were assumed to be unphysical when the absolute value of a component i of the electric field changed by more than 1 mV/km at time t , and the values $E_i(t-2)$ through $E_i(t+4)$ were replaced using linear interpolation of the values at $E_i(t-3)$ and $E_i(t+5)$. In the sample shown in Figure 2, 21 spikes were identified in E_x and zero in E_y . For the time intervals considered, the fraction of interpolated electric field values ranged from 0–0.1%.

The only modification made to the magnetic field measurements was the replacement of 36 data points on 2006-08-06 with linearly interpolated values. The 36 data points for B_x and B_y have the same value and are much larger than the surrounding values.

The GIC data contains nonphysical spikes that are followed by 40–80 s of anomalous values that appear as an exponential decay back to pre-spike values. These spikes were removed by identifying times t when the change in the 1 s absolute value of $GIC(t)$ was greater than 0.05 Amps and then values in a window $GIC(t-2)$ through $GIC(t+100)$ were replaced using a linear interpolation of the values at $GIC(t-3)$ and $GIC(t+101)$. In the example interval shown in Figure 2, 493 spikes were removed and approximately 15 spikes that were not removed by the automated algorithm are still visible. For the time intervals considered, the fraction of interpolated GIC values ranged from 1–4%.

3. Models and Methods

To determine the coefficients a_o and b_o in the frequency independent model, Model 1,

$$G_o(t) = a_o E_x(t) + b_o E_y(t) \quad (1)$$

the matrix equation $\mathbf{GIC} = \mathbf{E} \cdot \mathbf{p}$ is solved in a least squares sense, where \mathbf{GIC} is a zero mean 86400x1 matrix with rows of $GIC(t)$; $\mathbf{p} = [a_o, b_o]^T$, and \mathbf{E} is a 86400x2 matrix with rows of $[E_x(t), E_y(t)]$ with zero

mean columns. The values of a_o and b_o determined in this way correspond to those that minimize the sum-of-squares of $GIC(t) - G_o(t)$ over a 1-day interval. (Pulkkinen et al., 2007, provided the mathematically equivalent analytic equations for solving the matrix equation.) The notation \bar{a}_o and \bar{b}_o will be used for the average of the a_o and b_o values computed using 35 1-day-window-segment regressions.

In Model 2, the system coefficients $a(\omega)$ and $b(\omega)$ are frequency dependent (frequency-dependent variables are indicated by explicitly listing their dependence on ω):

$$G_E(\omega) = a(\omega)E_x(\omega) + b(\omega)E_y(\omega), \quad (2)$$

and were estimated using the Fourier transforms of $GIC(t)$ and $\mathbf{E}(t)$; the method of coefficient estimation and the generation of time-domain GIC estimates for this and the following models are given at the end of this section.

Motivated by the results described in the following section, in which Model 2 provides a significantly better representation of GIC than Model 1, we have also considered two additional models that can be used to estimate GIC. In these two models, a direct measurement of the geoelectric field is not used; instead, the driver is the geomagnetic field, which is much more often measured, and as a result, these models may be of practical interest.

In Model 3, previously computed coefficients $a(\omega)$ and $b(\omega)$ from Model 2 are used, but with an electric field \mathbf{E}' computed using the measured magnetic field, \mathbf{B} , and a transfer function $Z: \mathbf{E}'(\omega) \equiv Z(\omega)\mathbf{B}(\omega)$ and

$$G_{E'}(\omega) = a(\omega)E'_x(\omega) + b(\omega)E'_y(\omega), \quad (3)$$

where the electric field components are $E'x(\omega) = Z_{xx}(\omega)B_x(\omega) + Z_{xy}(\omega)B_y(\omega)$ and $E'y(\omega) = Z_{yx}(\omega)B_x(\omega) + Z_{yy}(\omega)B_y(\omega)$. That is, instead of using the measured electric field directly as in Model 2, a transfer function that relates $\mathbf{E}(\omega)$ to $\mathbf{B}(\omega)$ is used to provide an estimate of the electric field based on the magnetic field.

The fourth model is

$$G_B(\omega) = z_x(\omega)B_x(\omega) + z_y(\omega)B_y(\omega). \quad (4)$$

In this model, the transfer function components $z_x(\omega)$ and $z_y(\omega)$ are determined directly from measurements of $GIC(t)$ and $\mathbf{B}(t)$, and no electric field measurements are used; this model is expected to produce estimates of GIC that are similar to that obtained from Model 3 because they both use the same input measurements.

Estimates of $a(\omega)$ and $b(\omega)$ in Model 2 are made at evaluation frequencies, $\omega_e \equiv 2\pi f_e$, by performing an ordinary least squares regression (OLS). At each evaluation frequency, a regression is performed using a set $G_E(\omega)$, $E_x(\omega)$, and $E_y(\omega)$ values from the DFT (discrete Fourier transform) of 24 hr of 1-s cadence data in a band of frequencies around ω_e . Following the suggestion of Simpson and Bahr (2005), the 28 values of f_e start at 0.25 Hz and decrease by a factor of $\sqrt{2}$ and end at 1/43200 Hz; if a f_e value computed in this way is not an integer multiple of 1/86400, the nearest smaller integer multiple is used. The periods associated with the evaluation frequencies are listed in Table A2.

The same approach is used for solving for $z_x(\omega_e)$ and $z_y(\omega_e)$ in equation (4).

For the transfer function Z in $\mathbf{E}(\omega) = Z(\omega)\mathbf{B}(\omega)$ used in Model 3, the xx and xy components of Z at the evaluation frequencies are solved for using the same method used for Model 2 using the equation

$$E_x(\omega) = Z_{xx}(\omega)B_x(\omega) + Z_{xy}(\omega)B_y(\omega),$$

and the yx and yy components are solved for using

$$E_y(\omega) = Z_{yx}(\omega)B_x(\omega) + Z_{yy}(\omega)B_y(\omega).$$

Transfer functions were computed for each of the 1-day segments. The average transfer function magnitude and phase at a given evaluation frequency were obtained by averaging the segment values at that evaluation frequency.

To interpolate the frequency-domain transfer function components that are estimated at the evaluation frequencies onto the original DFT frequency grid (with a spacing of 1/86400 Hz), their real and imaginary

components were linearly interpolated individually. The interpolated transfer function coefficients were set to zero at frequencies higher than 0.375 Hz, and the transfer function estimate at $f = 0$ was set to zero before interpolation.

GIC time series were calculated by multiplication of the interpolated transfer function coefficients with the DFT of the 24-hr long and 1-s cadence model inputs and computing the inverse DFT (e.g., for Model 2, $G_E(\omega) = a^I(\omega)E_x(\omega) + b^I(\omega)E_y(\omega)$ was calculated, where the superscript I indicates the interpolated value, and then the inverse DFT of $G_E(\omega)$ was calculated to give the estimate of $G_E(t)$ on a 1 s time grid).

Several modifications to this basic procedure were considered. Robust regression (Egbert & Booker, 1986) with either a Huber weighting using a constant of 1.345 or bi-square weighting using a constant of 4.685, both with no hard-cutoff step. The commonly used constants provide 95% efficiency for Gaussian-distributed errors. Models were also computed using time domain pre-whitening (using a 10th-order Yule-Walker model computed using the model output), time domain tapering (using a Parzen window), and weighting the frequencies around each evaluation frequency using Parzen window weights. When using these additional procedures individually, we find that the conclusions made regarding the differences in each model's prediction ability do not change because the differences in each model's prediction performance are within the calculated uncertainty of the used method. Transfer function coefficients found using these modifications are generally within the error bars of those for the used procedure when the signal-to-noise ratio is above ~ 3 (corresponding to periods longer than ~ 30 s); at periods shorter than ~ 30 s, the electric field measurements are significantly influenced by the instrument response characteristics (Fujii et al., 2015), aliasing, and the computed values are also expected to be significantly biased due to a low signal-to-noise ratio.

4. Model Evaluation

Out-of-sample estimation quality metrics for each model on day D were determined by computing the average model coefficients using the other 34 days of data and then using these average coefficients to generate GIC time series and associated metrics on day D . This process was repeated to create a set of 35 out-of-sample prediction metrics for each model. In calculating the metrics, the first and last 10 min of the day were excluded to reduce the influence of transients at the start and end of the interval.

The performance of each model in estimating GIC was assessed using three metrics: the prediction efficiency, PE, the mean-squared-error (MSE) ratio, and the signal-to-noise ratio (SN).

The mean-squared-error for model m is

$$\text{MSE}_m = \frac{1}{N} \sum_{t=t_0}^{t_f} (GIC(t) - GIC_m(t))^2,$$

where $GIC_m(t)$ is the estimate from model m at time step t ; $t_0 = 600$ and $t_f = 85800$, so that sum is over one day of 1-second-cadence measurements excluding the first and last 10 min. The MSE ratio for model m is $\text{MSE}_1/\text{MSE}_m$.

The prediction efficiency, PE, is the "Case I" skill score described by Murphy (1988) and is calculated using

$$\text{PE}_m = 1 - \frac{\sum_{t=t_0}^{t_f} (GIC(t) - GIC_m(t))^2}{\sum_{t=t_0}^{t_f} (GIC(t) - \overline{GIC(t)})^2},$$

where $\overline{GIC(t)}$ is an average over the same time interval used in the summations. The PE is a measure of the skill of the model with respect to the variance in the predictand and it represents the fraction of the variance in the data that is predicted by the model (when $\text{PE} \geq 0$).

The average PE and the MSE ratios were computed by averaging the out-of-sample PEs and MSE ratios. The 95% confidence interval, CI, on the PE and MSE ratios were calculated using the bootstrap method (Zoubir & Boashash, 1998): 1,000 random samples (with replacement) of 17 of the 35 out-of-sample prediction metrics were used to compute the CIs. The typical difference between the limits when the confidence intervals were computed assuming the values were Gaussian-distributed was $\sim 2\%$.

The frequency-dependent signal-to-noise ratio for each 1-day segment at a given evaluation frequency is the ratio of the smoothed power spectrum value of $GIC(\omega_e)$ to the smoothed power spectrum value of the

Table 1
Out-of-Sample Model Performance Metrics for Model m

m Model	PE	95% CI	MSE_1/MSE_m	95% CI
2 $G_E(t) = a(\omega)E_x(t) + b(\omega)E_y(t)$	0.60	[0.54, 0.65]	1.8	[1.6, 2.0]
3 $G'_E(t) = a(\omega)Ex'(t) + b(\omega)Ey'(t)$	0.78	[0.76, 0.80]	3.1	[2.8, 3.4]
4 $G_B(t) = z_xB_x(t) + z_yB_y(t)$	0.83	[0.80, 0.85]	4.6	[3.8, 5.3]

MSE_1/MSE_m is the MSE ratio of Model 1 to that of Model m . The PE and MSE ratios are the average of 35 values and the confidence interval, CI, was determined from 1,000 bootstrap samples.

prediction error at that evaluation frequency. A smoothed spectrum was obtained by averaging the raw spectrum in the same frequency bands used for the regression described in section 3. The average signal-to-noise ratio at a given evaluation frequency is the average of the 35 out-of-sample signal-to-noise ratios at that frequency.

5. Results

The PE and MSE ratios are shown in Table 1. Figure 3 shows the predictions for each model in a 1-day interval selected because the value of the prediction efficiency for each model was in the same order as that shown in Table 1, that is, Model 1 has the lowest PE, and Model 4 has the highest. The large errors visible at the start and end of the time intervals are due to the transients discussed in section 4 and the first and last 10 min of each interval were omitted from metrics calculations.

The primary conclusions of this work follow from the results shown in Table 1: the frequency-dependent model, Model 2, is significantly better at estimating GIC than the frequency-independent model, Model 1;

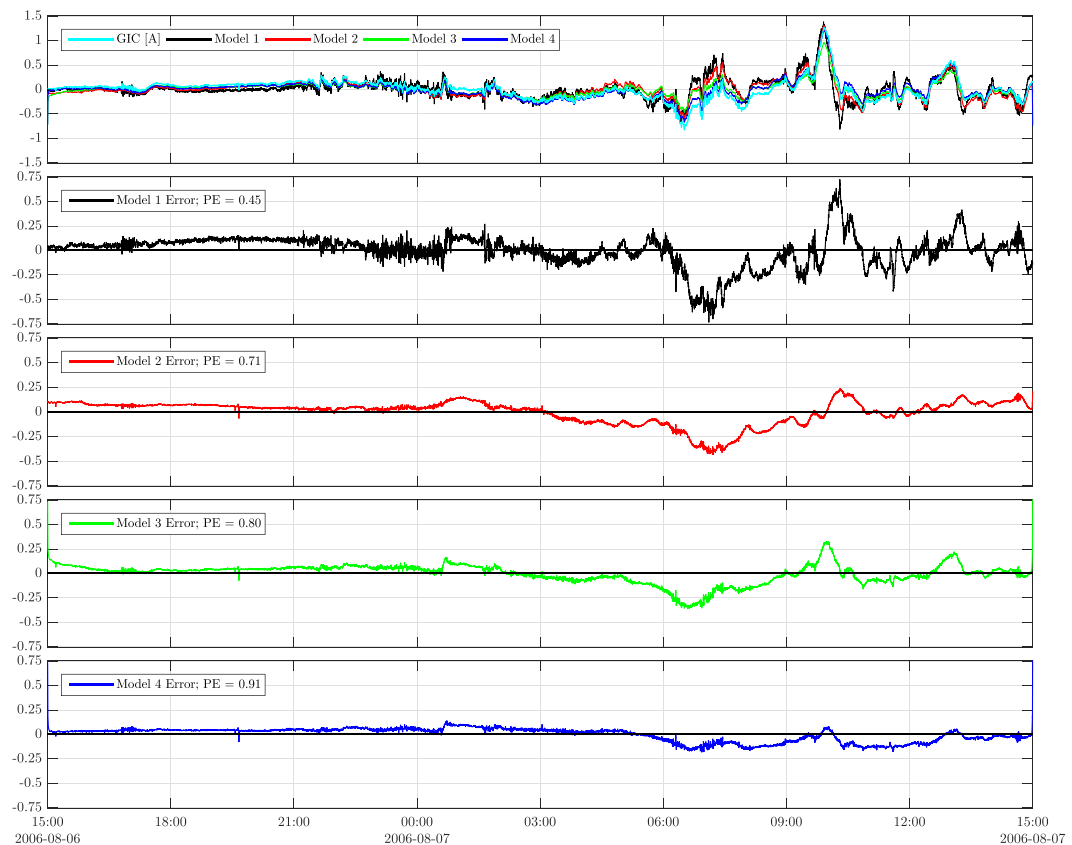


Figure 3. Out-of-sample model predictions (top) and predictions errors for each model in a selected 1-day interval. The scales for the error time series differ from that for the top panel so that the error amplitudes are scaled up by a factor of 2.

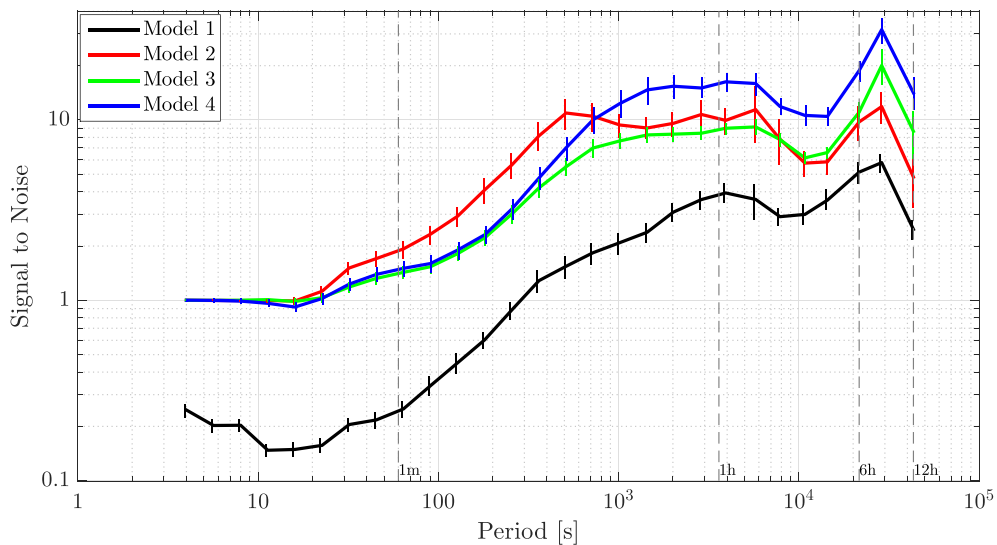


Figure 4. Out-of-sample signal-to-noise (signal to prediction error) ratios at the evaluation frequencies for the four models.

Model 3, which uses an estimate of the electric field based on magnetic field measurements, provides significantly better estimates of GIC than Model 2; Model 4, in which a transfer function that connects GIC to \mathbf{B} was derived directly from the data, provides better estimates of GIC than Model 3.

To determine the statistical significance of the PE differences, 10^5 bootstrap averages of the segment PEs of each model were created and their differences were computed. From this, the null hypothesis that the PE of Model 2 is equal to that of Model 1 can be rejected at a significance level of less than 10^{-5} because no bootstrap average PE difference from Model 2 was found to be lower than that for Model 1. The null hypothesis that the PE of Model 3 is equal to that of Model 2 can also be rejected at the same significance level. The null hypothesis that the PE of Model 4 is equal to that of Model 3 can be rejected at a significance level of 10^{-2} .

Figure 4 shows the average signal-to-noise (i.e., signal to prediction error) ratios as a function of period for the four models. At each evaluation frequency, the SN ratio is the ratio of the average of the out-of-sample SN ratios, and the error bars represent a 95% CIs based on 1,000 bootstrap samples of the segment SN ratios. Consistent with the results in Table 1, the SN ratio for Model 1 is lower than that for Models 2–4 at all frequencies. However, ordering of the SN ratio for Models 2–4 is dependent on period.

Below 600 s, Model 2 has the largest SN ratio. This result is somewhat visible in the sample interval shown in Figure 3 where the high-frequency fluctuations in the prediction error for Model 2 are the smallest among the models. Below 600 s, the predictive ability of each model is in the order that may be expected based on the data used to derive the model: Model 2, which uses direct measurements of the electric field, has a larger SN ratio than Model 3, which uses an indirect estimate of the electric field. Model 4 has a slightly larger SN than Model 3, and this is expected because they both use the same input of the magnetic field, but Model 3 has an additional source of uncertainty from the data-estimated coefficients in \mathbf{Z} .

Above 600 s, the ordering of the SN is not consistent with these expectations and is possibly explained by two factors: (1) the measured GIC is based on an integrated electric field along the power line, and the electric field used in Model 2 is a point measurement made 9 km away from the line—it follows that there is an implicit assumption in the model that the electric field is uniform over the length of the line on which GIC is measured; and (2) the error associated with this assumption has less of an influence on the errors in a model that uses point measurements of the magnetic field. Issues related to this are discussed in the following section.

Above 10,000 s (2.8 hr), the SN ratio ordering is the same as the ordering of the PE and MSE ratios shown in Table 1, with Model 1 having the lowest and Model 4 having the largest SN ratio.

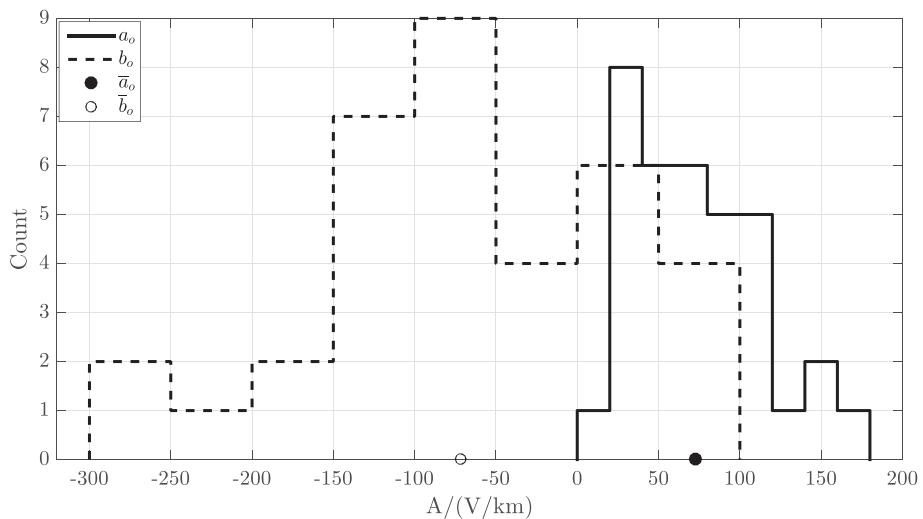


Figure 5. Distribution of coefficients in Model 1. Each set of coefficients was computed 35 times using one day of 1-second cadence data. The circle or dot on the horizontal axis indicates the average of a histogram and $\bar{a}_o = 73$ A/(V/km) and $\bar{b}_o = -72$ A/(V/km).

The average coefficients and 95% CI for Model 1 are $\bar{a}_o = 73.0$ [62, 83] A/(V/km) and $\bar{b}_o = -72.0$ [-98, -45] A/(V/km), and the distribution of the coefficients for the segments is shown in Figure 5. (Results are similar if 1-min averages are used; Watari (2015) found $a_o = 38.1$ A/(V/km) and $b_o = -7.4$ A/(V/km) for the interval 2006-12-14 to 2006-12-15 JST time interval).

The values of $\bar{a}_o = 73$ A/(V/km) and $\bar{b}_o = -72$ A/(V/km) and Model 1 imply that for a given electric field magnitude, GIC is largest at the measurement site when the electric field points 45° west of north, which is approximately perpendicular to the 187 kV line shown in Figure 1 that runs in the northeast direction. Pulkkinen et al. (2010) used magnetic field data at Memanbetsu and GIC data for a 3-day interval starting on 2005-12-26 and found a b_o/a_o ratio of -1.9/50, corresponding to a maximum GIC when the electric field angle is 2° west of north. The $b_o/a_o = -7.4/38.1$ ratio documented in Watari (2015) using data from a 2-day interval starting on 2006-12-14 that corresponds to an angle of 11° west of north.

The average coefficients for Models 2 and 4 are shown in Figures 6 and 7. The error bars at each period correspond to the standard error of the 35 values used to compute the average.

Figure 6 shows that the frequency domain transfer functions for Model 2 vary by an order of magnitude on timescales of 60 s to 12 hr (that for Model 1 is constant by definition). For this system, GIC is more sensitive to E_y than E_x due to $b(\omega) > a(\omega)$, but $E_y(t)$ has less variability than $E_x(t)$ - the variance in $E_x(t)$ is ~5x larger than $E_y(t)$ over the entire dataset (this is also visible in Figure 2).

The ratio of $|\bar{b}_o|/|\bar{a}_o|$ is approximately 1 for Model 1, and this can be compared with $|b(\omega)|/|a(\omega)|$ calculated using the lines for $|a(\omega)|$ and $|b(\omega)|$ shown in Figure 6. The ratio varies from 2.7 at $T = 30$ s to 1.6 at $T = 12$ h.

Figure 7 shows the transfer function coefficient phase angles. For Model 1, the phase angle is 0° for positive coefficients and 180° for negative coefficients by definition. The phases for $a(\omega)$ and $b(\omega)$ are frequency dependent. At $T = 12$ hr, the phases of $a(\omega)$ and $b(\omega)$ differ by 180°, and the associated signs are consistent with those of $\bar{a}_o > 0$ and $\bar{b}_o < 0$. At $T = 12$ hr, the values of $b(\omega)$ and $a(\omega)$ and Model 2 correspond to an electric field of 60° west of north being associated with the largest GIC.

Both Models 1 and 2 predict a maximum GIC when the electric field angle is significantly different from the angle of the 187 kV line. As discussed in the following section, this can be caused by other parts of the power network (the details of which are unavailable) making significant contributions to GIC and differences in ground conductivity in parts of the network that contribute to GIC.

Figures 8 and 9 show the magnitude and phase for the coefficients of Z used in Model 3. Note that transfer function coefficients shown in Figure 8 differ significantly from that of a layered slab conductivity model for which $Z_{xy} = -Z_{yx}$ and $Z_{xx} = Z_{yy} = 0$. The electric and magnetic field data from Memanbetsu, Japan were

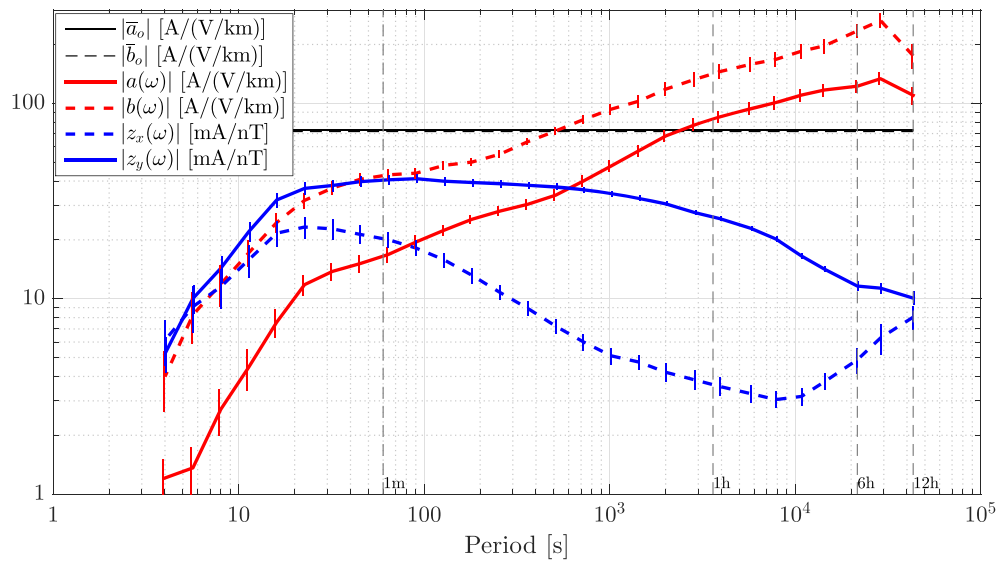


Figure 6. Frequency domain transfer functions for the coefficients in Models 1, 2, and 4. The frequency domain transfer functions for a_o and b_o in Model 1 are constant and equal to a_o and b_o .

also used by Fujii et al. (2015) to compute \mathbf{Z} . When using the Fujii et al. (2015) transfer function for Model 3, the PE was significantly lower (0.58 vs. 0.78). Although not critical to the conclusions in this work, a preliminary investigation suggests several explanations. We have found that when using continuous 1-month intervals prior to 2006 to compute \mathbf{Z} , our calculated transfer function coefficients match the Fujii et al. (2015) coefficients to within the error bars except below periods of 100 s, which is likely explained by the issues with the electric field response in the 1-second-cadence measurements discussed in Fujii et al. (2015) and the fact that we did not use a remote reference in our calculations. However, using 1-month intervals after 2006 (January through May tested), our calculated transfer function coefficient magnitudes differ significantly from that in Fujii et al. (2015)—they are shifted downward by approximately 10–50%. Also, we have found that the estimated transfer function is sensitive to whether or not segment averaging was used. Due to the large gaps between and the varying length of continuous segments of data used in this work, transfer

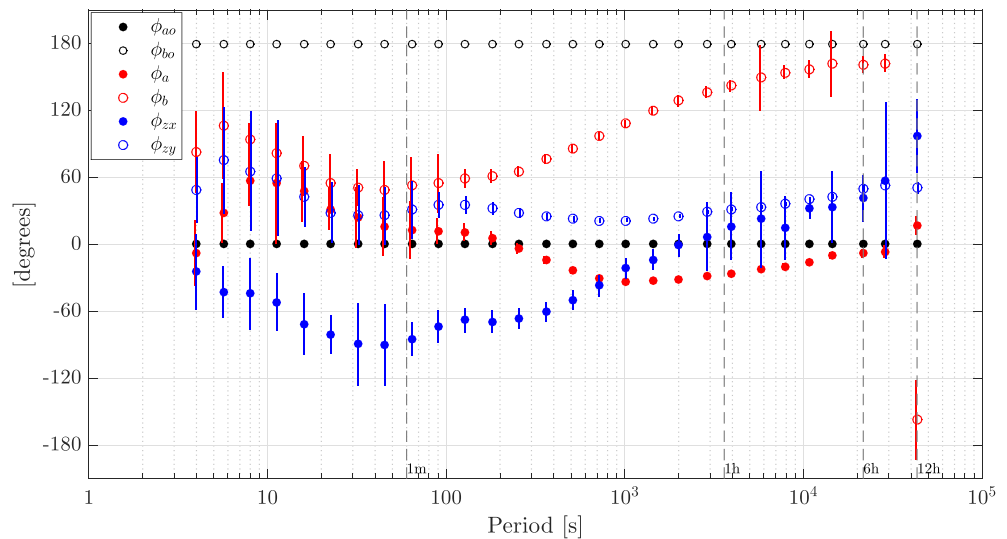


Figure 7. Frequency domain phase values for the coefficients in Models 1, 2, and 4. The phase for a_o and b_o are constant and either 0° or 180° depending on the sign of their value, with positive values having a phase of 0° .

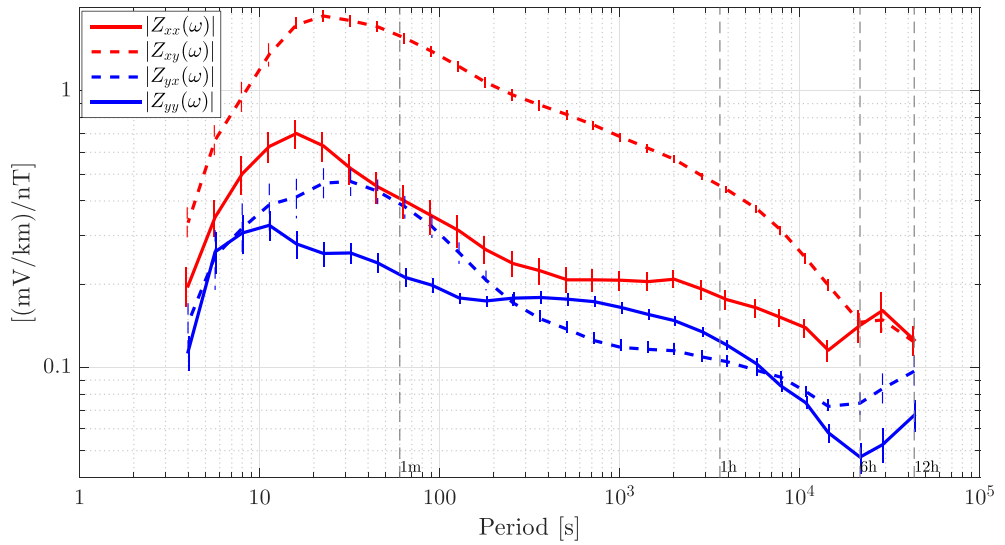


Figure 8. Frequency domain transfer functions for the **Z** coefficients used in Model 3.

functions were computed using 1-day segments of data and then averaged. We have found that if a continuous span of measurements over 21 days is used to compute a single transfer function, the transfer function coefficient magnitudes are up to 25% larger than if 21 transfer functions were computed and then averaged. This result is unexpected, and results from extensive verification tests of our MT calculations along with the fact that this effect has been observed by both authors using two different MT calculation codes on different data sets (the other code used was LEMI MT V1.4), suggests the explanation is not due to an error in the code used to compute the transfer functions in this work. This result suggests that stack averaging can be a significant source of transfer function bias and we expect that the explanation involves variations in the signal-to-noise between segments.

6. Discussion

There are at least three possible explanations for a frequency dependence in data-derived system coefficients: (1) the quasi-DC approximation is invalid, (2) it is an artifact of the measurement process, and (3) the electric field is not spatially and spectrally constant across the region of the power system.

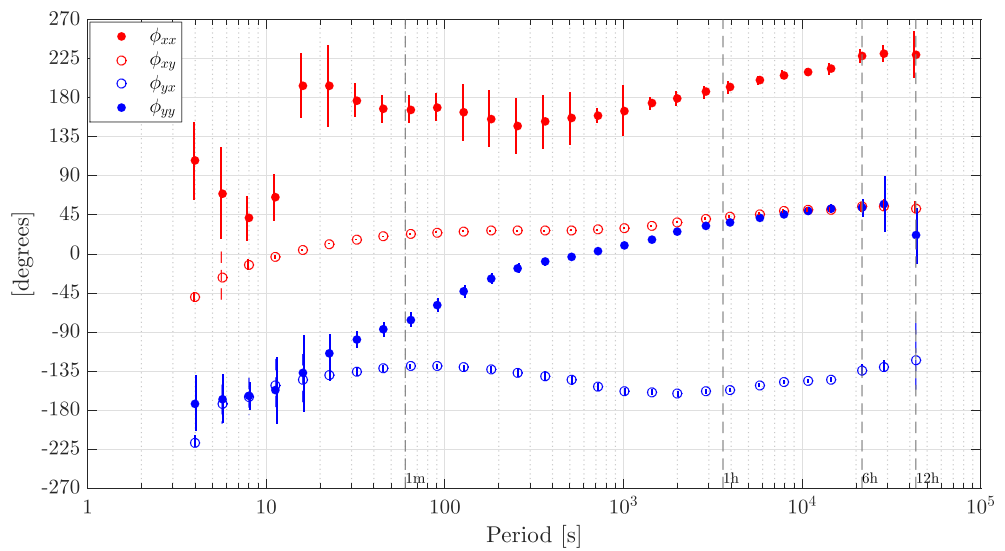


Figure 9. Frequency domain phase values for the **Z** coefficients used in Model 3.

(1) When the quasi-DC approximation is used, Albertson et al. (1981) is usually cited; their justification for the quasi-DC approximation is given in an appendix as “An analysis based on Carson’s equations reveals that transmission lines can be modeled for GIC determination by using their positive sequence resistance values with a small correction factor to account for skin and proximity effects. The correction factor varies from 0.95 to 1.0 depending on conductor size.” (Carson’s equations are equations for the impedance associated with a wire above an infinite and uniform half-space conducting slab (Carson, 1926; Grigsby, 2007) and positive sequence resistance values are the per phase line resistances in a balanced 3-phase power system.)

Lehtinen and Pirjola (1985) justifies the use of the quasi-DC approximation using the argument that GIC amplitudes are significant at frequencies that are much lower than the 50 Hz power line frequency. Clarified, this is essentially a statement that the reactance is proportional to frequency and although the reactance is typically ~ 5 times larger than the resistance at 50 Hz (Purchala et al., 2005), the reactance will be ~ 10 times smaller or less than the resistance at GIC frequencies of ~ 1 Hz and lower. Given these arguments, the quasi-DC approximation is justified, and an explanation involving a violation of the assumption of a uniform half-space conducting slab Earth using a conductivity that varies with depth to more accurately model skin and proximity effects also seems unlikely to explain the results as it would need to account for at least an order of magnitude of reactance. (However, Boteler, 1994 noted that for certain systems, the L/R time constant of the power network may be large enough to warrant inclusion in GIC flow calculations; this topic has more recently been pursued by Oyedokun et al., 2013.)

(2) A second consideration is that artifacts of the electric field and GIC measurements used in Model 2 cause the observed frequency dependence. However, the GIC instrument (HIOKI 9279 current sensor) is frequency independent to within $\pm 0.2\%$ in this period range and the response characteristics of the magnetic and electric field instruments are essentially frequency independent relative to the observed transfer function frequency dependence for periods in the range of $30 - 10^5$ s (Oowada et al., 1998; Fujii 2019 personal communication.)

(3) The coefficients in Model 1 are determined assuming that the electric field is spatially uniform at all points in the system. The exact calculation of GICs in a power system under the quasi-DC assumption requires knowledge of the electric field at all points of the system, and simulations of GIC flow typically start with an assumed electric field along the lines to calculate input voltages (Albertson et al., 1981; Lehtinen and Pirjola, 1985; Pirjola, 2009). The electric fields are then used along with the DC system component resistances and their connectivity to calculate GIC in the different parts of the system. In both Model 1 and Model 2, the input electric field is typically assumed to be spatially uniform along the line in which GIC was measured so that the induced voltage is directly proportional to the electric field. Spatial variations in the electric field measured on Earth’s surface can be due to horizontal variations in the incident electric field and horizontal variations in sub-surface conductivity, including those at land-ocean interfaces. If a spatial variation exists along the line in which GIC was measured, the coefficients derived from measurements in both models may differ significantly from those calculated using system configuration and resistance information. However, the data-derived coefficients will not have a frequency dependence that results only from the variation in the direction of a static electric field along the line.

The second assumption of Model 1 is that the spectrum of the electric field is uniform. Violation of this assumption can lead to an apparent violation of the quasi-static approximation. Consider an electric field and GIC that are measured at one end of a long line segment with the electric field being non-zero only at a frequency of ω_1 . If the electric field is spectrally uniform along the full line segment, then from the quasi-static approximation it follows that the measured GIC will also only be non-zero at a frequency of ω_1 . If the electric field at the other end of the line is non-zero only at a frequency of ω_2 , the observed GIC and electric field will appear to be inconsistent with the quasi-static approximation because GIC will have non-zero variations at both ω_1 and ω_2 .

To test the effect of different points on the line having different electric field spectra on the coefficient estimates, we created a simulated GIC signal using electric field measurements made in Memanbetsu (indicated with a superscript M) and Kakioka (superscript K), Japan:

$$G_s(t) = a_o [(1 - r)E_x^M(t) + rE_x^K(t)] + b_o [(1 - r)E_y^M(t) + rE_y^K(t)] \quad (5)$$

with $a_o = 1$, $b_o = -1$ and $r = 0.2$. G_s represents a simulated GIC in which 20% of the line has a different electric field. (The zero-lag cross correlation is -0.40 for $E_x^M(t)$ and $E_x^K(t)$ and 0.64 for $E_y^M(t)$ and $E_y^K(t)$). The model equation

$$G_s(\omega) = a(\omega)E_x^M(\omega) + b(\omega)E_y^M(\omega) \quad (6)$$

was then used to compute $a(\omega)$ and $b(\omega)$, and they were both found to exhibit a frequency dependence similar to that shown in Figure 6 in that they both have an increase in magnitude with period, although in this experiment the increase was a factor 2–6 for periods in the range of 2 s to 12 hr.

Although this proof-of-concept simulation shows how variations in the frequency content of the geoelectric field on the line in which GIC is measured can cause the data-estimated system coefficients to have a frequency dependence, it is very crude as it uses several approximations that were necessitated by the availability of data. The distance from Kakioka to Memanbetsu is $\sim 1,400$ km, which is ~ 14 x that of the length of the power line (~ 100 km) on which GIC was measured, and the correlations between the electric field from the two sites are likely to be lower than the fields measured at points separated by a distance closer to the length of the power line. In addition, the discontinuous change in the electric field implicit in the model implies that there would be a part of the line that can have a non-zero net charge and thus is not physically realizable for typical conductors. A more realistic simulation would use electric field measurements that were both near a line on which GIC was measured and separated from each other by a distance that is comparable to the length of the line.

In the discussion of (3) above, we have attempted to address independently the contribution of spatial variations in the electric field magnitude and direction and spatial variations in the electric field spectra, but generally these variations do not occur independently as they are both caused by horizontal variations in the ground conductivity. A time-varying ionospheric current can also cause spatial and spectral variations in the electric field magnitude (Boteler & Pirjola, 1998). Thus, the finding in section 5 that the angle of the electric field that produces maximum GIC differs significantly from the angle of the 187 kV power line for both Models 1 and 2 may be consistent with the frequency dependence of a and b found in Model 2. However, testing this claim would require a full network analysis, knowledge of the ground conductivity throughout the network, and accounting for the driving ionospheric currents.

7. Conclusions

The primary implications of the results presented are (1) significantly improved estimates of GICs using data-derived system coefficients a and b can be made if they are allowed to be frequency dependent, and (2) a and b coefficients derived using a traditional frequency-independent model may differ significantly from those computed using power system configuration information.

Although the use of frequency-independent a and b coefficients estimated from data give reasonable estimates of GIC, it is not known how much data-estimated coefficient values will differ from those directly calculated. (Due to the limited availability of details of the power system and the ground conductivity along the line, we were not able to make this comparison.) Works that use Model 1 and generally note a high degree of visual consistency between the measured values and predictions using this model (e.g., the top panel of Figure 3). However, we have shown using contemporaneous GIC and electric field measurements that a significantly better estimation of GIC can be obtained by using a frequency-dependent model of the form of Models 2 and 3.

When GIC and magnetic field measurements are available, a model of the form of Model 4 can be used. For this particular data set, we have found that such a model provides the best estimates of GIC in terms of the PE, MSE, and signal-to-error metrics. Local ground magnetic field estimates along with GIC measurements could be used to derive a transfer function model that is updated when the system configuration changes and this model could be used to estimate GIC under extreme or simulated geomagnetic conditions. A key advantage of this approach is that long-term geomagnetic field measurements are generally easier to make and more readily available than geoelectric field measurements. A disadvantage is the transfer function coefficients of Model 4 are difficult to interpret physically because they contain components of the transfer functions that connect the electric field to the magnetic field and GIC to the electric field.

A: Appendix

Table A1
Date Intervals used for Analysis

Start date	End date
2006-04-03	2006-04-10
2006-07-25	2006-07-29
2006-08-05	2006-08-08
2006-08-19	2006-08-21
2006-11-07	2006-11-12
2006-11-28	2006-11-29
2006-12-01	2006-12-14
2006-12-15	2006-12-15
2007-11-18	2007-11-20
2007-11-22	2007-11-22

Table A2
Periods Associated with Evaluation Frequency Bands used for Regression and Smoothing Spectra

#	N	T_e [s]	T_l [s]	T_h [s]
1	2	43200	28800	86400
2	2	28800	21600	43200
3	3	21600	14400	43200
4	4	14400	9600	28800
5	5	10800	7200	21600
6	6	7854.5	5400	14400
7	8	5760	3927.3	10800
8	12	3927.3	2618.2	7854.5
9	16	2880	1920	5760
10	22	2009.3	1350	3927.3
11	31	1440	960	2880
12	43	1016.5	680.3	2009.3
13	61	720	480	1440
14	85	511.2	341.5	1016.5
15	120	361.5	241.3	720
16	170	255.6	170.4	511.2
17	240	180.8	120.5	361.5
18	338	128	85.4	255.6
19	478	90.5	60.3	180.8
20	676	64	42.7	128
21	956	45.2	30.2	90.5
22	1351	32	21.3	64
23	1910	22.6	15.1	45.2
24	2701	16	10.7	32
25	3819	11.3	7.5	22.6
26	5401	8	5.3	16
27	7638	5.7	3.8	11.3
28	10801	4	2.7	8

Note. # is the evaluation frequency number, N is the number of DFT points in the band, and $T_e \equiv 1/f_e$. The band range is from T_l through T_h .

Acknowledgments

Magnetic and electric field measurements made at the Kakioka Magnetic Observatory were obtained from the Japan Meteorological Agency Data Portal <http://www.kakioka-jma.go.jp/obsdatalmetadata/en>. The geomagnetic coordinates in Figure 1 were computed using code from https://www.ngdc.noaa.gov/geomag/geom_util/apex.shtml. The Fujii et al. (2015) transfer function was obtained from the IRIS DMC EMTF database [Kelbert et al. (2011)]. We thank the Hokkaido Electric Power Co. for the GIC measurements at the Memanbetsu substation and Shinichi Watari for communicating and preparing the GIC data and providing feedback on the manuscript. We also thank Ikuko Fujii for providing clarifications on the geoelectric instrument response, Trevor Gaunt and Emanuel Bernabeau for review and comments on part (1) of section 6, and Josh Rigler for substantial feedback and review.

References

- Albertson, V., Bozoki, B., Feero, W., Kappenman, J., Larsen, E., Nordell, D., et al. (1981). Load-flow studies in the presence of geomagnetically-induced currents. *IEEE Transactions on Power Apparatus and Systems, PAS-100*(2), 594–607. <https://doi.org/10.1109/tpas.1981.316916>
- Albertson, V., Kappenman, J., Mohan, N., & Skarbakka, G. (1993). Geomagnetic disturbance effects on power systems. *IEEE Transactions on Power Delivery, 8*(3), 1206–1216. <https://doi.org/10.1109/61.252646>
- Boteler, D. H. (1994). Geomagnetically induced currents: present knowledge and future research. *IEEE Transactions on Power Delivery, 9*(1), 50–58. <https://doi.org/10.1109/61.277679>
- Boteler, D. H. (2014). Methodology for simulation of geomagnetically induced currents in power systems. *Journal of Space Weather and Space Climate, 4*, A21. <https://doi.org/10.1051/swsc/2014018>
- Boteler, D. H., & Pirjola, R. (1998). Modelling geomagnetically induced currents produced by realistic and uniform electric fields. *IEEE Transactions on Power Delivery, 13*(4), 1303–1308. <https://doi.org/10.1109/61.714500>
- Boteler, D. H., & Pirjola, R. (2014). Comparison of methods for modelling geomagnetically induced currents. *Annales Geophysicae, 32*(9), 1177–1187. <https://doi.org/10.5194/angeo-32-1177-2014>
- Boteler, D. H., & Pirjola, R. J. (2017). Modeling geomagnetically induced currents. *Space Weather, 15*, 258–276. <https://doi.org/10.1002/2016sw001499>
- Carson, J. R. (1926). Electric circuit theory and the operational calculus. *Bell System Technical Journal, 5*(2), 336–384. <https://doi.org/10.1002/j.1538-7305.1926.tb04305.x>
- Egbert, G. D., & Booker, J. R. (1986). Robust estimation of geomagnetic transfer functions. *Geophysical Journal International, 87*(1), 173–194. <https://doi.org/10.1111/j.1365-246x.1986.tb04552.x>
- Fujii, I., Okawa, T., Nagamachi, S., & Owada, T. (2015). The characteristics of geoelectric fields at Kakioka, Kanoya, and Memambetsu inferred from voltage measurements during 2000 to 2011. *Earth, Planets and Space, 67*(1). <https://doi.org/10.1186/s40623-015-0241-z>
- Gaunt, C. T. (2014). Reducing uncertainty – responses for electricity utilities to severe solar storms. *Journal of Space Weather and Space Climate, 4*, A01. <https://doi.org/10.1051/swsc/2013058>
- Grigsby, L. (Ed) (2007). *Electric Power Generation, Transmission, and Distribution*. Boca Raton, FL: CRC Press Taylor and Francis Group. <https://doi.org/10.1201/9781420009255>
- Horton, R., Boteler, D. H., Overbye, T. J., Pirjola, R. J., & Dugan, R. C. (2012). A test case for the calculation of geomagnetically induced currents. *IEEE Transactions on Power Delivery, 27*(4), 2368–2373. <https://doi.org/10.1109/tpwrd.2012.2206407>
- Kelbert, A., Egbert, G. D., & Schultz, A. (2011). Data services products: EMTF, The Magnetotelluric Transfer Functions, <https://doi.org/10.17611/dp/emtf1>
- Lehtinen, M., & Pirjola, R. (1985). Currents produced in earthed conductor networks by geomagnetically-induced electric fields. *Annales Geophysicae, 3*(4), 479–484.
- Liu, C., Li, Y., & Pirjola, R. J. (2014). Observations and modeling of GIC in the Chinese large-scale high-voltage power networks. *Journal of Space Weather and Space Climate, 4*, A03. <https://doi.org/10.1051/swsc/2013057>
- Marshall, R. A., Gorniak, H., Walt, T. V. D., Waters, C. L., Sciffer, M. D., Miller, M., et al. (2013). Observations of geomagnetically induced currents in the australian power network. *Space Weather, 11*, 6–16. <https://doi.org/10.1029/2012sw000849>
- Molinski, T. S. (2002). Why utilities respect geomagnetically induced currents. *Journal of Atmospheric and Solar-Terrestrial Physics, 64*(16), 1765–1778. [https://doi.org/10.1016/s1364-6826\(02\)00126-8](https://doi.org/10.1016/s1364-6826(02)00126-8)
- Murphy, A. H. (1988). Skill scores based on the mean square error and their relationships to the correlation coefficient. *Monthly Weather Review, 116*(12), 2417–2424. [https://doi.org/10.1175/1520-0493\(1988\)116<2417:ssbotm>2.0.co;2](https://doi.org/10.1175/1520-0493(1988)116<2417:ssbotm>2.0.co;2)
- NERC (2012). Special reliability assessment interim report: Effects of geomagnetic disturbances on the bulk power system.
- Ngwira, C. M., McKinnell, L.-A., & Cilliers, P. J. (2011). Geomagnetic activity indicators for geomagnetically induced current studies in South Africa. *Advances in Space Research, 48*(3), 529–534. <https://doi.org/10.1016/j.asr.2011.03.042>
- Ohtani, S., Fujii, R., Hesse, M., & Lysak, R. L. (Eds.) (2000). *Magnetospheric Current Systems*. Washington, DC: American Geophysical Union. <https://doi.org/10.1029/gm118>
- Oowada, T., Tokumoto, T., Yamada, Y., Ozima, M., Kumazaka, N., Yokoyama, M., et al. (1998). Introduction to our new system: Magnetometer for wide frequency range. *Memoirs of the Kakioka Magnetic Observatory, 26*(2), 1–14.
- Overbye, T. J., Hutchins, T. R., Shetye, K., Weber, J., & Dahman, S. (2012). Integration of geomagnetic disturbance modeling into the power flow: A methodology for large-scale system studies. In *2012 North American Power Symposium (NAPS)*. IEEE. <https://doi.org/10.1109/naps.2012.6336365>
- Oyedokun, D., Simon, M., & Gaunt, C. (2013). Introduction of a more detailed calculation of geomagnetically induced currents in transmission networks. In *Proc. of Southern African Universities' Power Engineering Conference* (pp. 211–215). Potchefstroom, South Africa: Aconf.
- Pirjola, R. J. (2009). Properties of matrices included in the calculation of geomagnetically induced currents (GICs) in power systems and introduction of a test model for GIC computation algorithms. *Earth, Planets and Space, 61*(2), 263–272. <https://doi.org/10.1186/bf03352906>
- Pulkkinen, A., Kataoka, R., Watari, S., & Ichiki, M. (2010). Modeling geomagnetically induced currents in Hokkaido, Japan. *Advances in Space Research, 46*(9), 1087–1093. <https://doi.org/10.1016/j.asr.2010.05.024>
- Pulkkinen, A., Pirjola, R., & Viljanen, A. (2007). Determination of ground conductivity and system parameters for optimal modeling of geomagnetically induced current flow in technological systems. *Earth, Planets and Space, 59*(9), 999–1006. <https://doi.org/10.1186/bf03352040>
- Purchala, K., Meeus, L., Dommelen, D. V., & Belmans, R. (2005). Usefulness of DC power flow for active power flow analysis. In *IEEE Power Engineering Society General Meeting, 2005* (Vol. 1, pp. 454–459). IEEE. <https://doi.org/10.1109/pes.2005.1489581>
- Richmond, A. D. (1995). Ionospheric Electrodynamics Using Magnetic Apex Coordinates. *Journal of Geomagnetism and Geoelectricity, 47*, 191–212. <https://doi.org/10.5636/jgg.47.191>
- Simpson, F., & Bahr, K. (2005). *Practical Magnetotellurics* (p. 270). Cambridge, UK: Cambridge University Press. <https://doi.org/10.1017/cbo9780511614095>
- Stening, R. J., & Winch, D. E. (2013). The ionospheric sq current system obtained by spherical harmonic analysis. *Journal of Geophysical Research: Space Physics, 118*, 1288–1297. <https://doi.org/10.1002/jgra.50194>
- Thomson, A., Gaunt, C., Cilliers, P., Wild, J., Opperman, B., McKinnell, L.-A., et al. (2010). Present day challenges in understanding the geomagnetic hazard to national power grids. *Advances in Space Research, 45*(9), 1182–1190. <https://doi.org/10.1016/j.asr.2009.11.023>

- Viljanen, A., Pirjola, R., Wik, M., Ádám, A., Prácsér, E., Sakharov, Y., & Katkalov, J. (2012). Continental scale modelling of geomagnetically induced currents. *Journal of Space Weather and Space Climate*, 2, A17. <https://doi.org/10.1051/swsc/2012017>
- Watari, S. (2015). Estimation of geomagnetically induced currents based on the measurement data of a transformer in a Japanese power network and geoelectric field observations. *Earth, Planets and Space*, 67(1). <https://doi.org/10.1186/s40623-015-0253-8>
- Watari, S., Kunitake, M., Kitamura, K., Hori, T., Kikuchi, T., Shiokawa, K., et al. (2009). Measurements of geomagnetically induced current in a power grid in Hokkaido, Japan. *Space Weather*, 7, S03002. <https://doi.org/10.1029/2008sw000417>
- Wik, M., Viljanen, A., Pirjola, R. J., Pulkkinen, A., Wintoft, P., & Lundstedt, H. (2008). Calculation of geomagnetically induced currents in the 400 kV power grid in southern Sweden. *Space Weather*, 6, S07005. <https://doi.org/10.1029/2007sw000343>
- Zheng, K., Boteler, D. H., Pirjola, R. J., Liu, L., Becker, R., Marti, L., et al. (2014). Effects of system characteristics on geomagnetically induced currents. *IEEE Transactions on Power Delivery*, 29(2), 890–898. <https://doi.org/10.1109/tpwrd.2013.2281191>
- Zoubir, A., & Boashash, B. (1998). The bootstrap and its application in signal processing. *IEEE Signal Processing Magazine*, 15, 56–76. <https://doi.org/10.1109/79.647043>